

Supplementary Material:

Microscopic Mechanism of Water-Assisted Diffusional Phase Transitions in Inorganic Metal Halide Perovskites

Jialin Liu,¹ Xiangming Hao,¹ Marijn A. van Huis,² and Zhaochuan Fan¹

¹*Suzhou Institute of Nano-Tech and Nano-Bionics, Chinese Academy of Sciences,
Suzhou 215123, P. R. China*

²*Soft Condensed Matter, Debye Institute for Nanomaterials Science, Utrecht University,
3584CC Utrecht, The Netherlands*

(*Electronic mail: zcfan2021@sinano.ac.cn)

1. COMPUTATIONAL METHODS

1.1 MD simulations

All classical molecular dynamics (MD) simulations were performed using the GROMACS software package¹. The velocity Verlet algorithm² was used for the time integration with a time step of 2.0 fs. Throughout the simulations, the temperature and pressure of the system were controlled using the Nosé-Hoover thermostat and barostat, respectively³. The rigid ion model (RIM) for CsPbI₃⁴ and the SPC/E water model⁵ were utilized in classical MD simulations to investigate the role of water in the Y→B phase transition in CsPbI₃. The SPC/E model treated water molecules as rigid bodies. The non-bonded interactions between ions were described by short-range Lennard-Jones (LJ) potential and long-range Coulomb interaction:

$$\begin{aligned} U(r_{ij}) &= U_{\text{LJ}} + U_{\text{Coul}} \\ &= 4\epsilon_{ij} \left[\left(\frac{\sigma_{ij}}{r_{ij}} \right)^{12} - \left(\frac{\sigma_{ij}}{r_{ij}} \right)^6 \right] + \frac{q_i q_j}{r_{ij}} \end{aligned} \quad (1)$$

where q is the partial charge; ϵ and σ are the LJ parameters. The LJ parameters for different ion pairs were determined using the Lorentz–Berthelot (LB) mixing rule:

$$\begin{aligned} \epsilon_{ij} &= \sqrt{\epsilon_{ii} \epsilon_{jj}} \\ \sigma_{ij} &= (\sigma_{ii} + \sigma_{jj}) / 2 \end{aligned} \quad (2)$$

A cutoff radius of 1.2 nm was employed for the LJ potential, and the potential energy was globally shifted to ensure zero energy at the cutoff radius. Long-range Coulomb interactions were calculated using the Fast Smooth Particle-Mesh Ewald (SPME) method⁶, with a real-space cutoff of 1.2 nm and reciprocal space computed using FFTs. The electrostatic force accuracy was maintained at $2\text{-}3 \times 10^{-4}$. Force field parameters for the CsPbI₃-water system are listed in Table S2. The RIM for CsPbI₃ has been rigorously tested in previous studies, demonstrating its accuracy in describing solid properties and solid-solid phase transitions, including the transitions from γ - β - α and α - δ solid phases, as well as the melting of α -CsPbI₃⁷. Given that our rigid ion model assumes ionic charges of $q_{\text{Cs}} : q_{\text{Pb}} : q_{\text{I}} \neq 1 : 2 : -1$, it presents challenges in accurately simulating the complex process of CsPbI₃ decomposition into CsI and PbI₂. For future simulation studies of such processes, we recommend employing more sophisticated and advanced models, such as ReaxFF⁷ and machine learning force fields (MLFFs)⁸. Details of the force field validation for the combination of the SPC/E water model and CsPbI₃ RIM are discussed in Section 2.

1.2 Calculation of interfacial energy

In the construction of a black/yellow (B/Y) interface, the γ -(001) surface contacts with the δ -(100) surface, and the γ -[100] and the δ -[100] directions are parallel to the long axis of the nanowire (Fig. S1a). The black γ phase belongs to the $Pmna$ space group, with lattice parameters of $a = 8.70 \text{ \AA}$, $b = 9.00 \text{ \AA}$, and $c = 12.77 \text{ \AA}$. The yellow δ phase belongs to the $Pmnb$ space group, with lattice parameters of $a = 5.08 \text{ \AA}$, $b = 10.50 \text{ \AA}$, and $c = 17.87 \text{ \AA}$. We constructed the B/Y interface using relatively large supercells for both phases: $7 \times 14 \times 14$ for the black phase and $12 \times 12 \times 10$ for the yellow phase. With these supercells, the lattice mismatch was negligible under periodic boundary conditions. The structure was equilibrated for 10 ns at 300 K and 1 atm.

In the construction of a crystal/amorphous (C/A) interface (Fig. S1b-c), we first melted a $6 \times 6 \times 4$ supercell of the γ phase and a $10 \times 5 \times 3$ supercell of the δ phase at a high temperature of 1500 K to form the amorphous blocks. During the simulations, the y and z axes of the simulation boxes were held constant, and the x axis was relaxed to control the pressure at 1 atm. Subsequently, the system was cooled down to 300 K at a rate of 50 K/ns and relaxed at 300 K for 1 ns to achieve a glass state. The crystal and amorphous systems were combined along the x direction, with a gap of 7 \AA . By relaxing at 100 K and 1 atm for 0.5 ns, the crystal and amorphous blocks were tightly contacted, forming the C/A interfaces. Two atomic layers near the C/A interfaces were relaxed at 1000 K for 0.5 ns and then cooled down to 300 K at a rate of 100 K/ns. Finally, the system was equilibrated for 10 ns at 300 K and 1 atm.

To investigate the impact of water molecules on interfacial energy, disordered systems containing water molecules were constructed (Fig. S1d-e). To accommodate the distinct lattices of the black and yellow phases, two amorphous + water blocks were created: one comprising 896 CsPbI₃ units with 253 water molecules in a $10 \times 72.88 \times 62.8 \text{ nm}^3$ simulation box, and the other comprising 600 CsPbI₃ units with 170 water molecules in a $8.50 \times 5.30 \times 5.45 \text{ nm}^3$ simulation box. The amorphous + water blocks were initially equilibrated at 1500 K and 1 atm for 0.5 ns, with the y and z axes held constant. Subsequently, the systems were cooled down to 300 K at a rate of 100 K/ns and relaxed for 10 ns at 300 K. The construction of the two-phase system followed the same procedure as the water-free system.

To validate the force field, we constructed smaller interface structures for MLFF-accelerated AIMD simulations. We constructed supercell structures for the B/Y interface with dimensions of $2 \times 1 \times 4$ for the γ phase and $12 \times 1 \times 1$ for δ phase, aimed to minimize lattice mismatch

across the interface. For the γ -phase, the lattice constants were set $a = 9.0329 \text{ \AA}$, $b = 10.4694 \text{ \AA}$, $c = 12.4377 \text{ \AA}$. For the δ -phase, the lattice constants were set $a = 4.1459 \text{ \AA}$, $b = 9.0329 \text{ \AA}$, $c = 18.0658 \text{ \AA}$. The interfaces for the B/A and Y/A structures were constructed using identical methods, annealing temperatures, and conditions. These structures will be used for comparison and analysis in subsequent simulations. These interface structures underwent relaxation in the NPT ensemble at a simulation temperature of 300 K and a pressure of 1 atm. Ab initio molecular dynamics (AIMD) simulations, accelerated by on-the-fly MLFF for 20 ps, were conducted, with the final 5 ps used for energy sampling. Detailed methodological aspects of the MLFF-accelerated AIMD simulations are provided in Section 1.9 of the supplementary information.

The results show that the interface energies obtained from AIMD simulations are in close agreement with those from classical molecular dynamics (MD) simulations (see Table I). This agreement validates the accuracy of the classical force field in describing interface energy and reinforces the reliability of our conclusions."

The total energies of the crystal, amorphous, amorphous + water, and two-phase systems were sampled from the last 2 ns of the simulations. The interfacial energy can be calculated using the formula:

$$\sigma = \frac{(n_1 + n_2)e_{\text{tp}} - (n_1e_1 + n_2e_2)}{2A} \quad (3)$$

Where e_{tp} is the per ion total energy of the two-phase system, and e_1 and e_2 are the per ion total energies of the two systems that constitute the two-phase system. n_1 and n_2 represent the number of ions in the two systems. A is the interfacial area, and the factor of 2 accounts for the presence of two equivalent interfaces in the two-phase systems. The calculated interfacial energies are listed in Table I. As shown in Fig. S2b and S2c, the transition from the disordered phase to the yellow phase is significantly accelerated in simulations with water molecules compared to those without. This notable increase in the phase transformation rate rules out the possibility of a solely seeded growth mechanism.

1.3 Model constructions of nanowires

Three different nanowire systems were constructed: the black phase (space group $Pm\bar{3}m$, lattice parameter $a = 6.217 \text{ \AA}$), the yellow phase (space group $Pmnb$, lattice parameters $a = 4.991 \text{ \AA}$, $b = 10.38 \text{ \AA}$, $c = 17.156 \text{ \AA}$), and a structure composed of half black phase and half yellow phase (B-Y). All nanowires have a length of 16 nm and a diameter of 8 nm. The [100] crystallographic

direction was aligned parallel to the nanowire’s long (x) axis for the nanowires with pure black and yellow phases. For the B-Y nanowire, simulations were conducted to model the contact between the (100) facets of the black phase and yellow phase⁹. To minimize large dipole moments, half of the cations at the cation-terminated surface of the black phase were moved to the other interface. In all three systems, various numbers of water molecules (0, 500, 1000, 1500) were placed near the nanowire surface. An initial separation of 1.0 nm was maintained between the black and yellow phases. Subsequently, this structure was equilibrated for 10 ns at 300 K and 1 atm, allowing the black and yellow phases to spontaneously come into contact and undergo structural reorganization at the interface to achieve an equilibrium conformation. During the simulations, the temperature was controlled at 300 and 600 K. Pressure control was applied only along the z -direction to ensure minimal deformation of the simulation box. 1 μ s molecular dynamics (MD) simulation was performed for each nanowire system.

1.4 Model constructions of B-Y two-phase bulk systems

In the two-phase bulk systems (Fig. S4), the fraction of the ions in the yellow phase is approximately 62%. The contact at the B/Y interface was consistent with that of the nanowire. Considering the relatively small system size and the use of the periodic boundary conditions, there was a certain degree of lattice mismatch and internal stress that is inevitable in the B/Y two-phase bulk system. To mitigate these effects, a $4 \times 7 \times 6$ supercells of the black phase (with lattice parameters of $a = 12.98 \text{ \AA}$, $b = 9.06 \text{ \AA}$, $c = 9.1 \text{ \AA}$) were connected to a $15 \times 6 \times 3$ supercells of the yellow phase (with lattice parameters of $a = 5.2 \text{ \AA}$, $b = 10.57 \text{ \AA}$, $c = 18.2 \text{ \AA}$), controlling lattice mismatch and internal stress within 1% and 0.03 GPa, respectively. Similarly, half of the cations at one interface were moved to the other to minimize dipole moments. As depicted in Fig. S4, 0, 50, 100, and 150 water molecules were added at the B/Y interface (corresponding to 0, 25, 50, and 75 water molecules per interface). With an interface area of 34.63 nm^2 , the water content was converted to interfacial water areal density ρ . The interfacial water densities for the 0-, 50-, 100-, and 150-water systems are 0, 0.72, 1.45, and 2.17 nm^2 , respectively. The systems were first heated from 300 K to a high temperature (520-620 K) under the NPT ensemble to achieve equilibrium at the B/Y interface without apparent phase transitions. Subsequently, simulations were conducted at high temperatures (700, 710, 720 K) for 1.5 μ s.

1.5 Crystal structure identification

In CsPbI₃ materials, we employed the Interval Common Neighbor Analysis (I-CNA) method¹⁰ nested within the OVITO software¹¹ to identify the body-centered cubic (bcc) sublattice structure formed by cations (Pb and Cs) in the black phase. In this phase, the cationic sublattice (Pb and Cs) exhibit a bcc structure. Furthermore, this approach enables us to quantitatively determine the proportion of the black phase within the material. To ascertain the lattice type, the investigation examines the quantity of near-neighbor atoms shared by the central atom, the number of bonds between these shared near-neighbor atoms, and the length of the longest chain of atoms formed by these shared near-neighbor atoms. For the bcc structure, a thorough analysis is conducted on both the nearest and second-nearest neighbor atoms. The bcc structure must satisfy specific conditions, including six shared near-neighbor atoms, six bonds between these shared near-neighbor atoms, and six atoms in the longest chain formed by these shared near-neighbor atoms. Additionally, the bcc structure should exhibit four shared near-neighbor atoms, four bonds between these shared near-neighbor atoms, and four atoms in the longest chain formed by these shared near-neighbor atoms.

The selection of the cutoff radius in this method plays an important role in accurately identifying near-neighbor atoms. The method systematically inserts possible cutoff radii in ascending order (from the shortest to the longest) and evaluates their compatibility with the reference structure. By exhaustively enumerating all conceivable threshold selections, it becomes feasible to plot the interval of cutoff radii where the structure remains invariant. Note that this method encounters limitations in clearly distinguishing between the yellow phase and the disordered phase.

1.6 Transition rate and transition barrier

In the calculations of the phase transition barriers, ten independent simulations were performed for each system at different temperatures. The time evolution of the fraction of the black phase was sampled in each simulation (Fig. S5). To observe significant Y→B phase transitions in simulations spanning a few hundred nanoseconds to microsecond range, simulations were performed at high temperatures (700, 710, and 720 K) above the transition point. Due to notable differences in transition rates at varying water contents and temperatures, different simulation times were selected for calculating transition rates in each system. Results from 150 ns simulations were used

for sampling for the systems undergoing rapid transitions, while 1.5 μ s simulations were used for those undergoing slower transitions. For each simulation, the phase transition rate (v) was defined as:

$$v = \frac{L}{2} \frac{d(n_B/n_{\text{tot}})}{dt} \quad (4)$$

Where L is the length of the x -axis of the simulation box, n_B is the number of ions with the black phase, and n_{tot} is the total number of ions. The phase transition rate for each system was the average of the rates from the ten independent simulations (Fig. S5). The transition barriers were obtained by the Arrhenius fit:

$$v = A \exp(-\Delta E_{\text{tran}}/k_B T) \quad (5)$$

the slope of the linear fit of $\ln v$ over $1/T$ is the phase transition energy barrier (ΔE_{tran}).

1.7 Diffusion coefficient of interfacial ions and diffusion barrier

The mean square displacement (MSD) of I ions was used as an order parameter to determine the position of the B/Y interface accurately for calculating the diffusion rate and diffusion energy barrier of interface ions. The MSD of I ions at the interface is larger than within the MSD of I ions at the crystal ($\sim 0.03 \text{ nm}^2$). To precisely locate the interface position, we analyze trajectories from 200 ps MD simulations. The interface does not exhibit significant movement in this relatively short time frame. Fig. S8 displays the average MSD of I ions at different x -coordinates across ten independent simulations, indicating that the accurate position of the B/Y interface can be precisely determined using this method.

For statistical analysis of diffusion rates, 50 independent simulations were conducted for each system, with each simulation running for 2 ns. The initial 0.4 ns were used for equilibration, while the last 1.6 ns were used for sampling. The diffusion coefficient (D) was calculated using the formula:

$$D = \frac{1}{6} \frac{d\text{MSD}}{dt} \quad (6)$$

The diffusion energy barrier was determined by the Arrhenius fit:

$$D = A' \exp(-\Delta E_{\text{diff}}/k_B T) \quad (7)$$

the slope of the linear fit of $\ln(D)$ against $1/T$ is the diffusion energy barrier (ΔE_{diff}). Fig. S6 shows the time evolution of the RMSD of interfacial ions with different ρ and at different T and Fig. S7 shows the linear fit of $\ln(D)$ over $1/T$ with different ρ .

1.8 Coordination number analysis

The method in the preceding section was used to locate the B/Y interface. We used the radial distribution function ($g(r)$) of interfacial ions to determine the cutoff distance for analyzing the coordination numbers. The cutoff distances used for various ion pairs are listed in Table III. For ions in the B/Y interface region, we calculated the average number of ions or water oxygen within the cutoff radius for each ion, thus obtaining the coordination number. Data were sampled from 10 independent simulations, and 500 frames of the trajectory in each simulation were used to calculate the coordination number.

1.9 AIMD and MLFF-accelerated AIMD simulations

Ab initio molecular dynamics (AIMD) simulations were conducted using the Vienna ab initio Simulation Package (VASP) with the projected augmented wave (PAW) method^{12,13}. The generalized gradient approximation (GGA) with the Perdew, Burke, and Ernzerhof (PBE) exchange-correlation functional was employed, along with the D3 method of Grimme et al. and Becke-Johnson (BJ) damping for van der Waals correction^{14,15}. This hybrid functional, PBE-D3(BJ), has been demonstrated to accurately reproduce the relative stability of CsPbI₃ polymorphs¹⁶. The plane wave cutoff energy was set to 500 eV, and only the Γ point was used for the k -points. Seven systems were constructed for AIMD simulations: 32CsPbI₃ in the γ , δ , and amorphous structures (Fig. S10a-c), and these structures with four water molecules (Fig. S10d-e). Additionally, a system with only four water molecules in a $\sim 2 \times 2 \times 2$ nm³ simulation box was considered (Fig. S10j).

Simulations were performed in the NPT ensemble using the Langevin thermostat, and the Parrinello-Rahman method controlled temperature and pressure¹⁷. However, the simulation was conducted in the NVT ensemble for the system with only four water molecules. AIMD simulations for systems with water molecules comprised 10,000 steps (5 ps) with a timestep of 0.5 fs, while simulations for systems without water utilized 5,000 steps (10 ps) with a longer timestep of 2.0 fs. The intercalation energy of a water molecule in an 8CsPbI₃ system is defined as:

$$E_{\text{form}} = \frac{1}{4} (E_{32\text{CsPbI}_3+4\text{H}_2\text{O}} - E_{32\text{CsPbI}_3} - E_{4\text{H}_2\text{O}}) \quad (8)$$

where $E_{32\text{CsPbI}_3+4\text{H}_2\text{O}}$, $E_{32\text{CsPbI}_3}$, and $E_{4\text{H}_2\text{O}}$ represent the total energies of the systems with 32CsPbI₃ and four water molecules, 32CsPbI₃ without four water molecules, and four water molecules alone, respectively. The last 2.5 ps of simulations were utilized for sampling.

In our interface simulations, due to the large number of atoms in the systems and the extended time required to reach equilibrium, we employed MLFF-accelerated AIMD simulations implemented in VASP^{18,19}. The exchange-correlation functional used in DFT calculations was PBE-D3(BJ)^{14,15}, with an energy cutoff of 450 eV. The k -point grid was restricted to the Γ point. For MLFF acceleration, we only set “ML_LMLFF=.TRUE.”, keeping all other parameters at their default values. This configuration allowed for the simultaneous training of a MLFF during MD simulations, with Bayesian error estimates determining on-the-fly whether DFT-level calculations or updates to the MLFF were needed^{18,19}. The potential energy surface of the MLFF was described by a modified Gaussian approximation potential (GAP)²⁰, while the system’s descriptors were based on a variant of smooth overlap of atomic positions (SOAP)^{18,19}. Simulations were performed in the NPT ensemble using the Langevin thermostat, and the Parrinello-Rahman method controlled temperature and pressure¹⁷. AIMD simulations were performed 10,000 steps with a timestep of 2 fs, and the last 5 ps of simulations were used for sampling.

2 FORCE FIELD VALIDATION

When conducting MD simulations using a RIM to explore the $B \leftrightarrow Y$ phase transitions in CsPbI_3 , we operate under two key assumptions: (1) Given the fixed charges in the force field, we presume that there are no alterations in the ionic oxidation states or substantial charge transfers among various ions during the $B \leftrightarrow Y$ phase transitions in the CsPbI_3 system²¹. (2) Direct μs -level MD simulations, which do not perturb system dynamics, can only reproduce the $Y \rightarrow B$ phase transition in CsPbI_3 under high-temperature conditions. We posit that the microscopic mechanisms governing the phase transitions near the transition point and at elevated temperatures are analogous.

Previous investigations have established the accuracy of the force field used in this study to describe various physical properties of CsPbI_3 , including crystal structures, melting points, and phase transition points⁷. A detailed evaluation of the CsPbI_3 force field is not provided here. Essential data related to the phase transitions of CsPbI_3 are summarized in Table IV. It’s worth noting that prior works based on density functional theory (DFT) and machine-learning force fields (MLFF) have proposed distinct transition pathways for the $B \leftrightarrow Y$ phase transition in CsPbI_3 ^{18,22–24}. In this study, we employ the force field to compute the energies of metastable and transition states in the multi-step phase transition pathway proposed by Chen et al.²². The results presented in

Fig. S9 indicate that the classical force field slightly overestimates the overall energy barrier for the phase transition and the relative energy value of the gamma phase. Nevertheless, the relative energy changes of metastable and transition states along the multi-step phase transition pathway, calculated using the classical force field, align with DFT results²².

Regarding the interaction between CsPbI₃ and water, we initially utilized the commonly employed Lorentz-Berthelot (LB) mixing rule to determine Lennard-Jones (LJ) parameters between CsPbI₃ ions and water molecules. To validate their accuracy, we conducted force field validation from three perspectives. First, we compared the intercalation energies of a water molecule in different CsPbI₃ systems at 300 K obtained from MD and AIMD simulations (Fig. S10). Fig. S11 demonstrates that the classical force field accurately predicts the order of E_{form} in different CsPbI₃ structures: $E_{\text{form}}^Y > E_{\text{form}}^B > E_{\text{form}}^A$. These results are consistent with MD simulations for CsPbI₃ nanowires, indicating that water molecules readily enter the amorphous B/Y interface but rarely penetrate the black or yellow crystal regions.

Subsequently, AIMD simulations were performed for the 32CsPbI₃+4H₂O systems at high temperatures of 500 and 700 K. In all simulations, water molecules neither decomposed nor underwent chemical reactions with CsPbI₃. This observation aligns with differential scanning calorimetry experiments, affirming that water molecules act as catalysts in accelerating the B \leftrightarrow Y transitions in CsPbI₃ without forming H₂O adduct²¹. This supports the use of MD simulations with RIM to comprehend the mechanisms of water-assisted Y \rightarrow B transition in CsPbI₃.

Finally, we considered the impact of changes in water-Cs, Pb, and I ion interactions on our simulation conclusions. In RIM, interatomic interactions are sensitive to changes in the value of the solvent-solute LJ parameter σ and ϵ ^{25,26}. We have conducted an extended investigation into the impact of modulating the water-Cs, Pb, and I ion intercalation energy (Fig. S15), specifically the σ and ϵ values, on the phase transformation rates (Fig. S16). In general, compared with LJ parameter ϵ , intercalation energy is more sensitive to the change of σ . As for different structures, the influence of σ on the intercalation energy of water in the amorphous CsPbI₃ structure is higher than that in the CsPbI₃ crystals. Our findings reveal that adjusting either the σ or ϵ within a $\pm 10\%$ range exerts negligible influence on the computed phase transformation rates. This observation underscores the robustness and high degree of reliability of the selected force field parameters in accurately depicting the phase change dynamics within this system (Fig. S16) We scaled the values of σ between water oxygen and Cs, Pb, and I ions by 0.9 and 1.1, respectively. Using the scaled force field parameters, we performed MD simulations and calculated the rate of Y \rightarrow B

phase transition of CsPbI₃ at 700 K (Fig. S12). The results indicate that scaling the water-ion σ value by $\pm 10\%$ does not significantly affect the transition rate. Therefore, we conclude that the mechanism of water molecules accelerating CsPbI₃ phase transitions obtained from our MD simulations is not sensitive to the water-ion interaction parameters. Overall, our CsPbI₃-water force field accurately captures the physics in the phase transitions and correctly describes the role of interfacial water molecules.

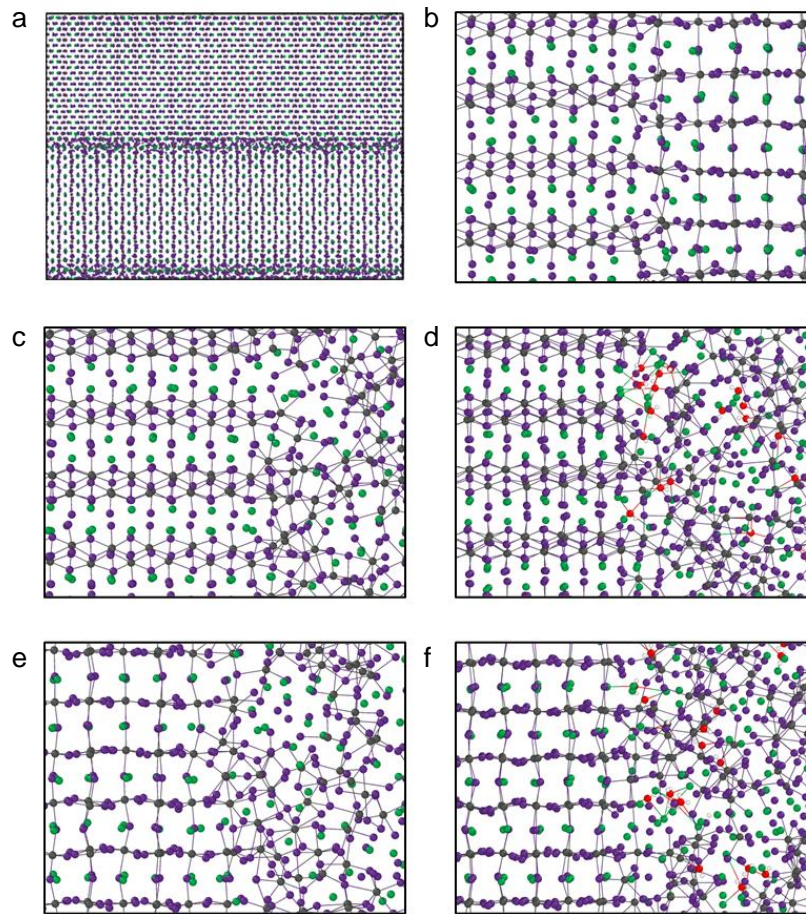


FIG. S1. **Structures of different CsPbI_3 interfaces from MD simulations.** (a) yellow/black (Y/B), (b) yellow/black (Y/B), (c) yellow/amorphous (Y/A), (d) yellow/amorphous with water molecules (Y/A+W), (e) B/A, and (f) B/A+W interface. Green, gray, purple, red, and white spheres are Cs, Pb, I, O, and H, respectively.

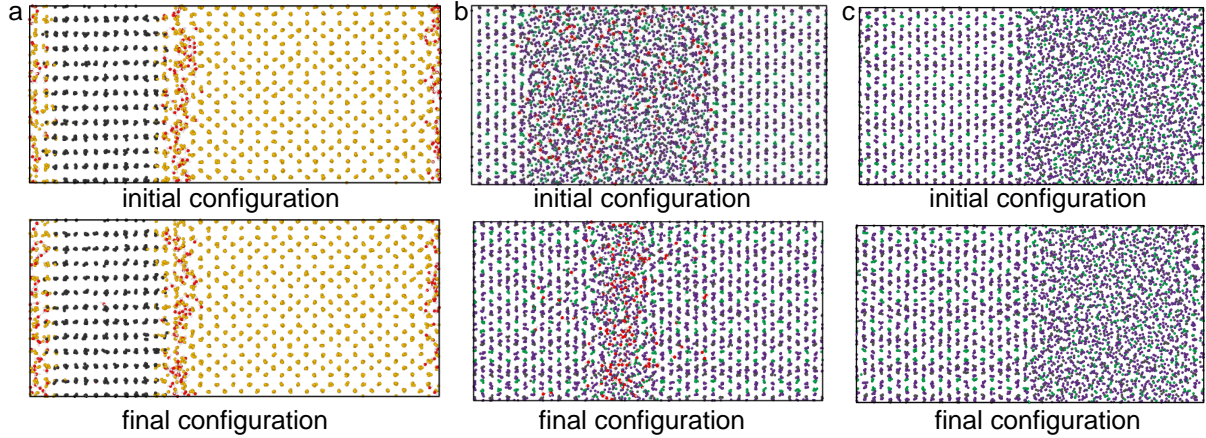


FIG. S2. **Microsecond-MD simulations for the phase transitions in CsPbI₃ with water molecules.** (a) Initial and final configurations of a two-phase bulk system with 200 water molecules in $2\text{-}\mu\text{s}$ MD simulations at 380 K. Only cations are shown for CsPbI₃, with gray indicating the black phase and yellow indicating the yellow phase or amorphous structure. No apparent B \rightarrow Y transformation was found in these microsecond-MD simulations due to the slow dynamics of this transition. (b) Initial and final configurations of a two-phase bulk system (Y/A+w) with 1500 water molecules and (c) two-phase bulk system (Y/A) in $2\text{-}\mu\text{s}$ MD simulations at 550 K. Green, gray, purple, red, and white spheres are Cs, Pb, I, O, and H, respectively.

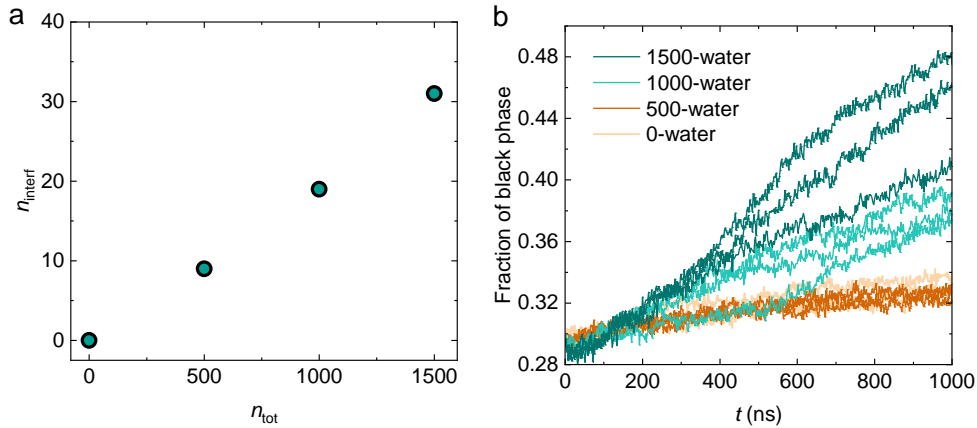


FIG. S3. **Influence of water on the B \rightarrow Y phase transition in CsPbI₃ nanowires.** (a) Relationship between the number of water molecules entering the interface (n_{interf}) and the total number of water molecules (n_{tot}). (b) Time evolution of the fraction of the black phase during the B-Y nanowire phase transition at 600 K for systems with different water contents. Three independent simulations were performed for each system.

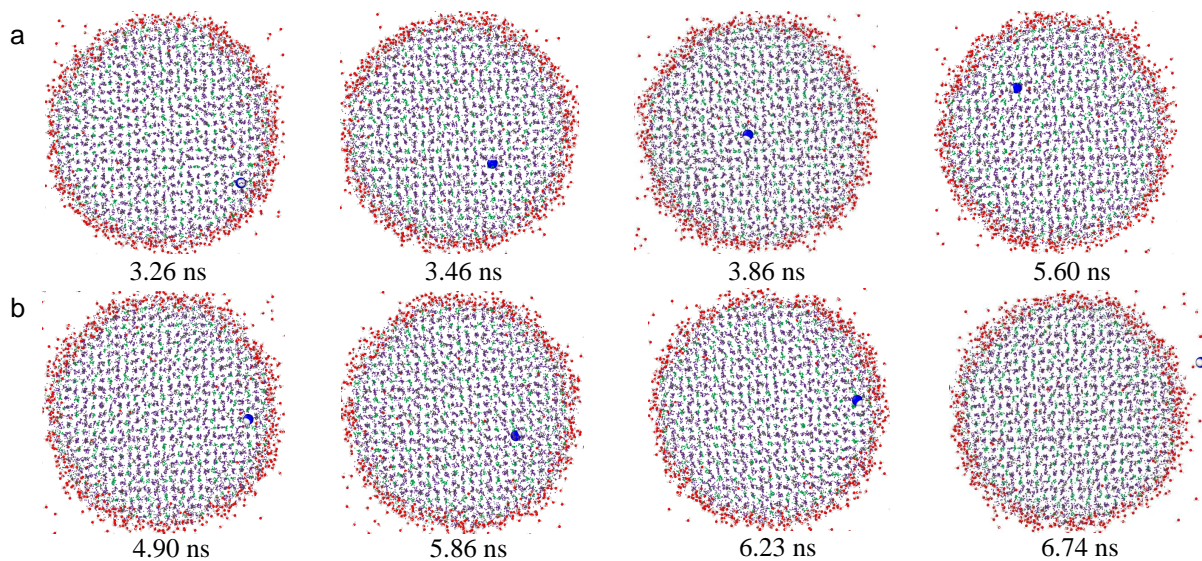


FIG. S4. The trajectories of water molecules for (a) entering the interface and (b) for exiting the interface.

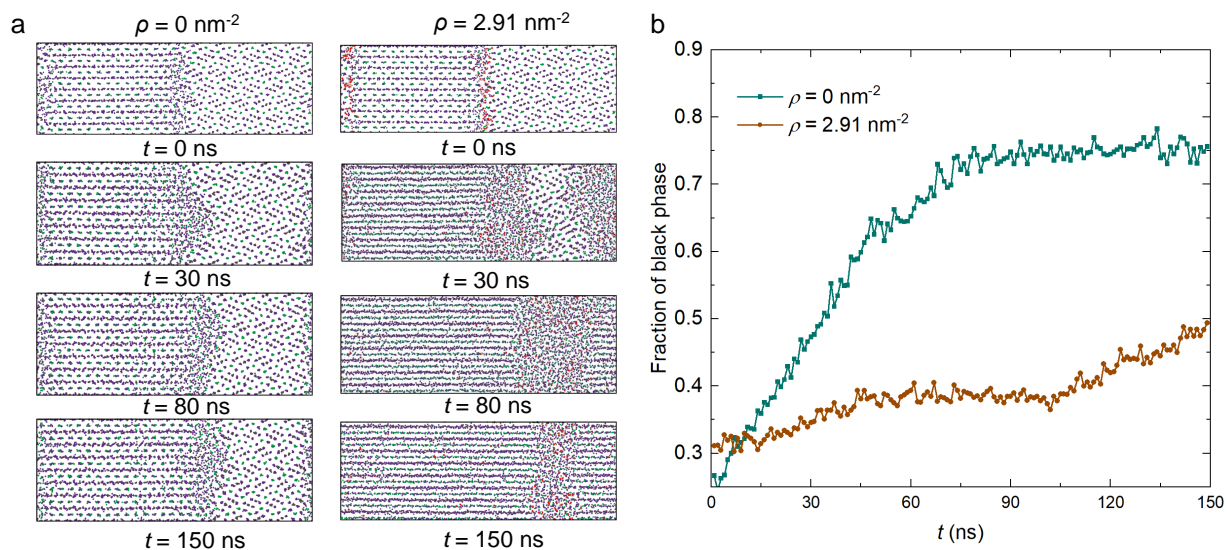


FIG. S5. **MD simulations for the B-Y bulk systems with different water contents.** The configuration of (a) zero-, 150-water systems at different time. Simulations were performed at 700 K for 150 ns. Green, gray, purple, red, and white spheres are Cs, Pb, I, O, and H, respectively. (b) Time evolution of the fraction of the black phase during the B/Y bulk (the γ -(010) surface contacts with the δ -(010) surface) phase transition at 700 K for systems with different water contents.

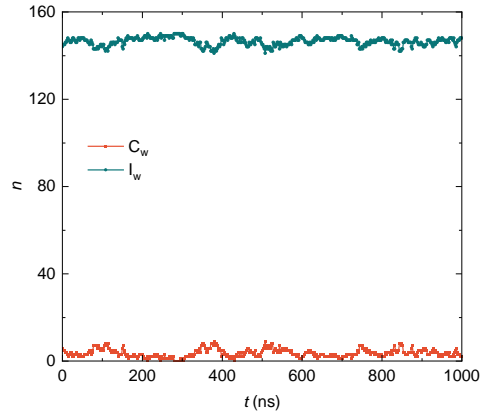


FIG. S6. Time evolution of the number of water molecule at interface and crystal with time over time at 700 K during the Y \rightarrow B phase transition.

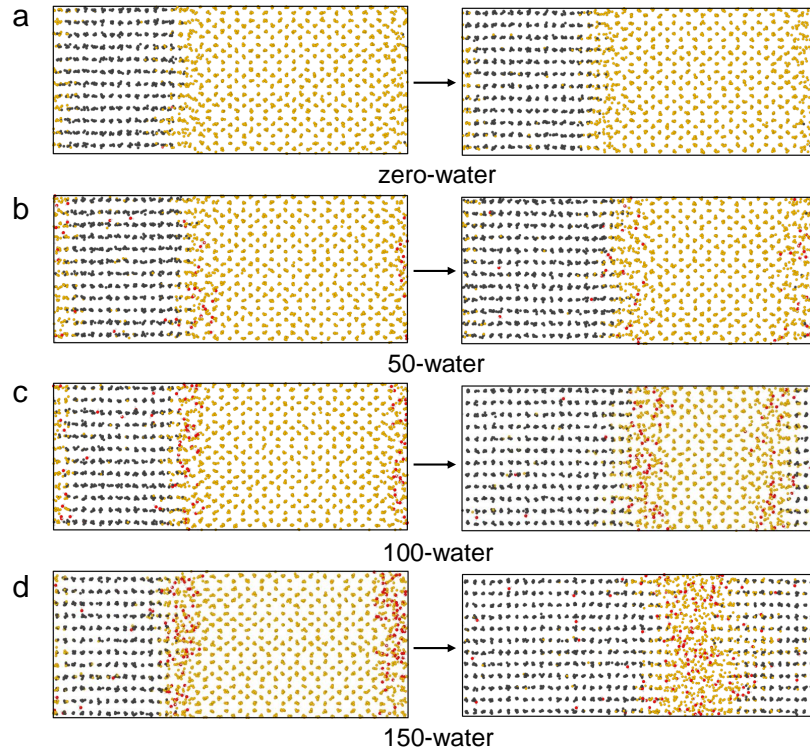


FIG. S7. **Initial and final configurations of MD simulations for the B-Y bulk systems with different water contents.** (a) zero-, (b) 50-, (c) 100-, (d) 150-water systems. For clarity, only cations are shown in CsPbI₃ nanowires, with gray indicating the black phase and yellow indicating the yellow phase or amorphous structure. Simulations were performed at 710 K for 320 ns.

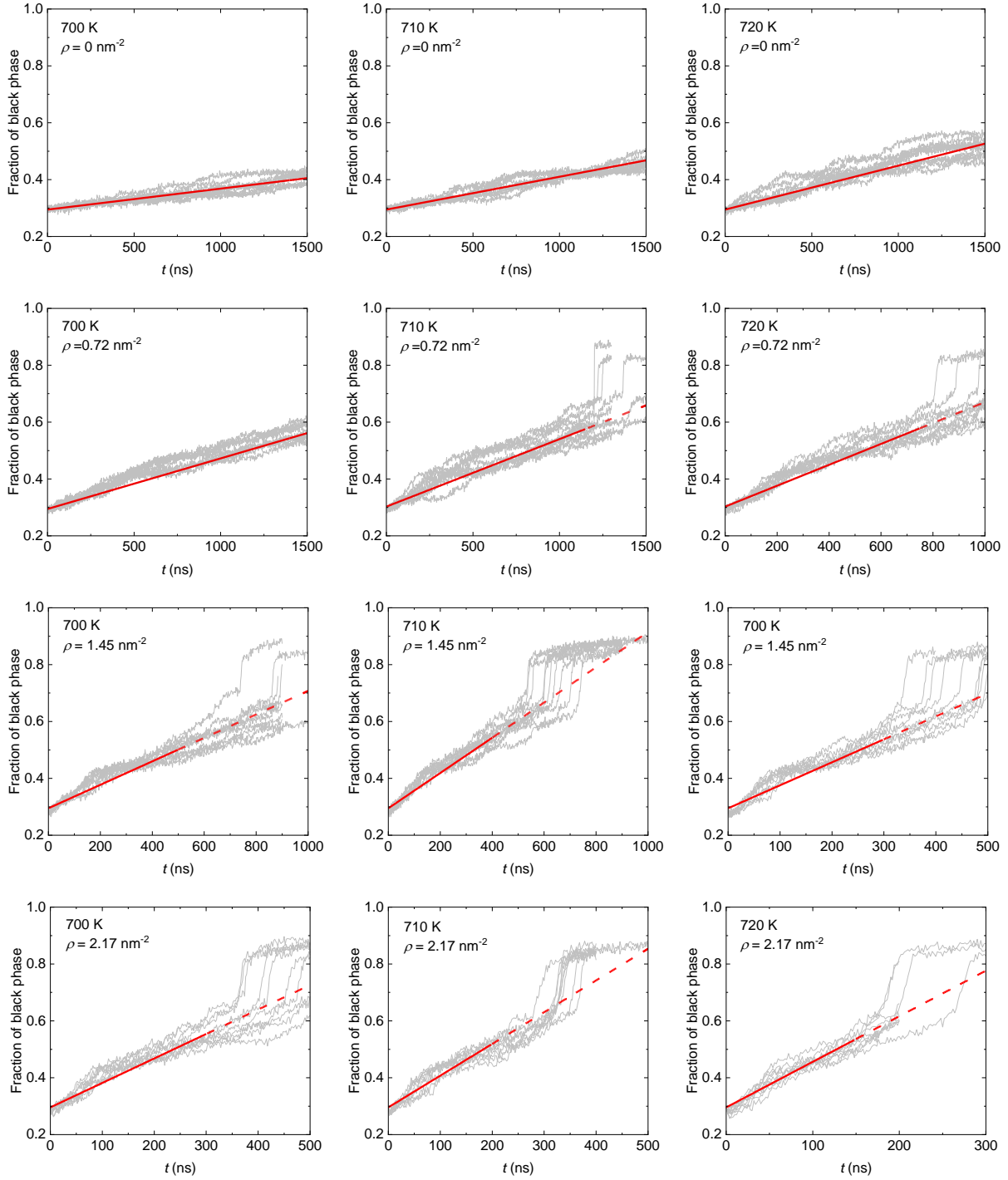


FIG. S8. Time evolution of the fraction of black phase in B-Y bulk systems with different water contents at different temperatures. The ten gray lines represent ten independent simulations, and the red line is the linearly fitted average, with the solid line indicating the sampling interval.

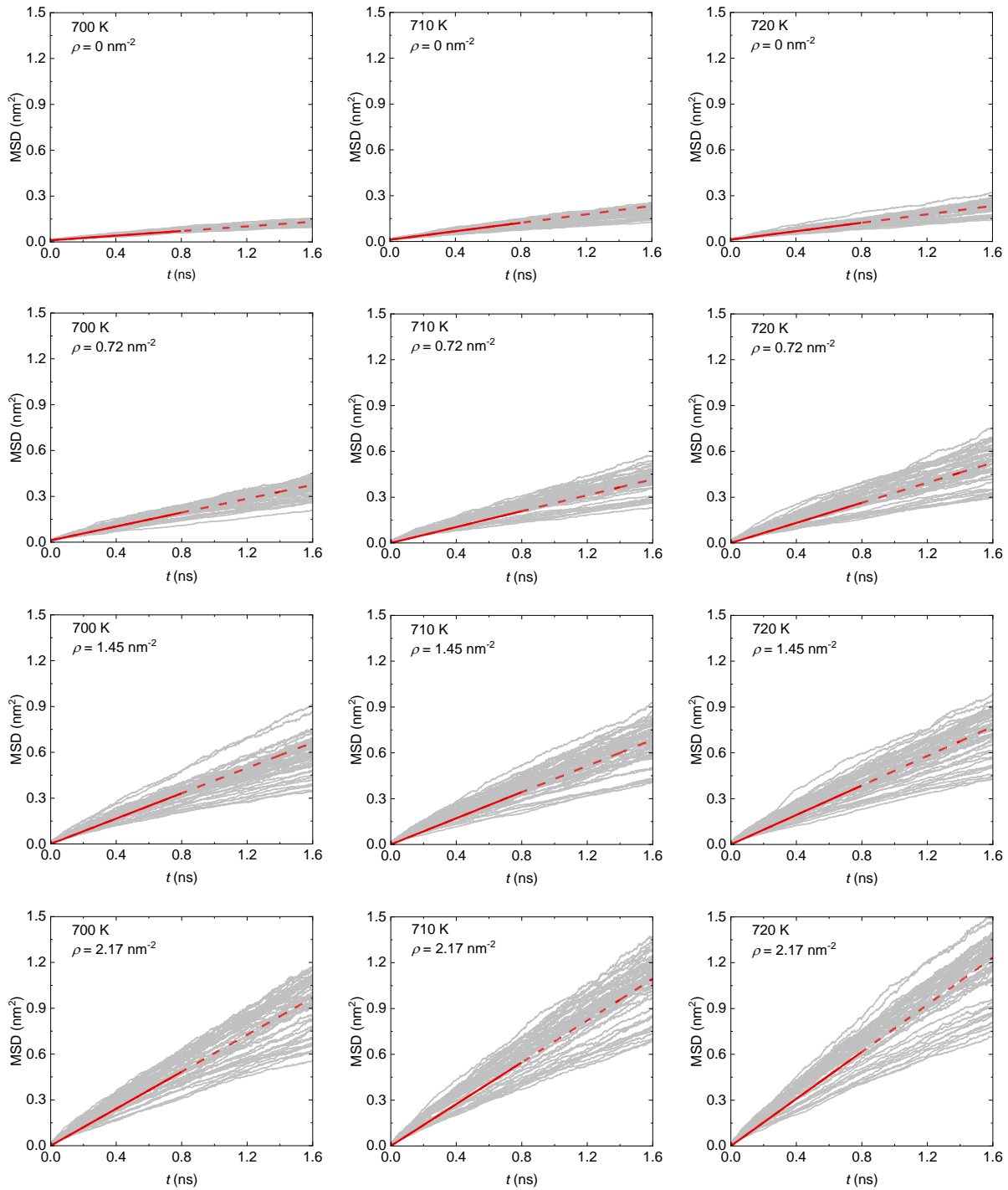


FIG. S9. Time evolution of interface ion MSD in B-Y bulk systems with different water contents at different temperatures. The 50 gray lines represent 50 independent simulations, and the red line is the linearly fitted average, with the solid line indicating the sampling interval.

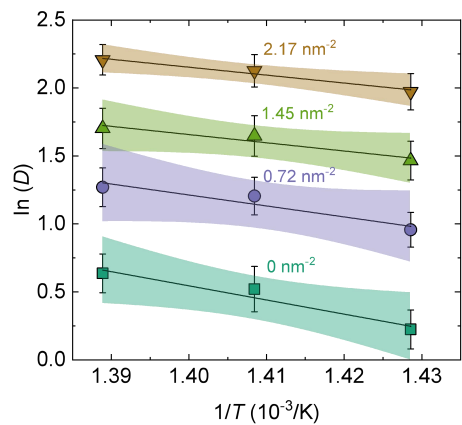


FIG. S10. Arrhenius plot of the diffusion barriers of interface ions in B-Y bulk systems with different water contents. The shaded region indicates the 85% confidence interval of the fit.

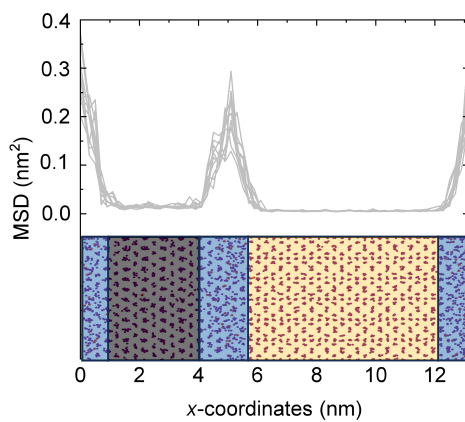


FIG. S11. Determination of the interface region. Average MSD of I ions at different x -coordinate positions in 10 independent simulations.

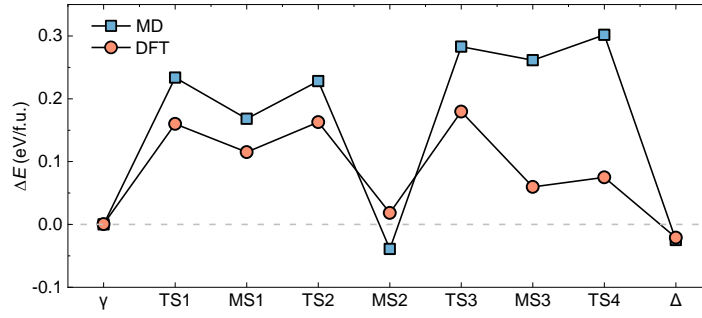


FIG. S12. Relative energy of metastable states and transition states in the proposed multistep C-C phase transition pathway, calculated using classical force field used in this work, compared with DFT calculations (Ref. 22).

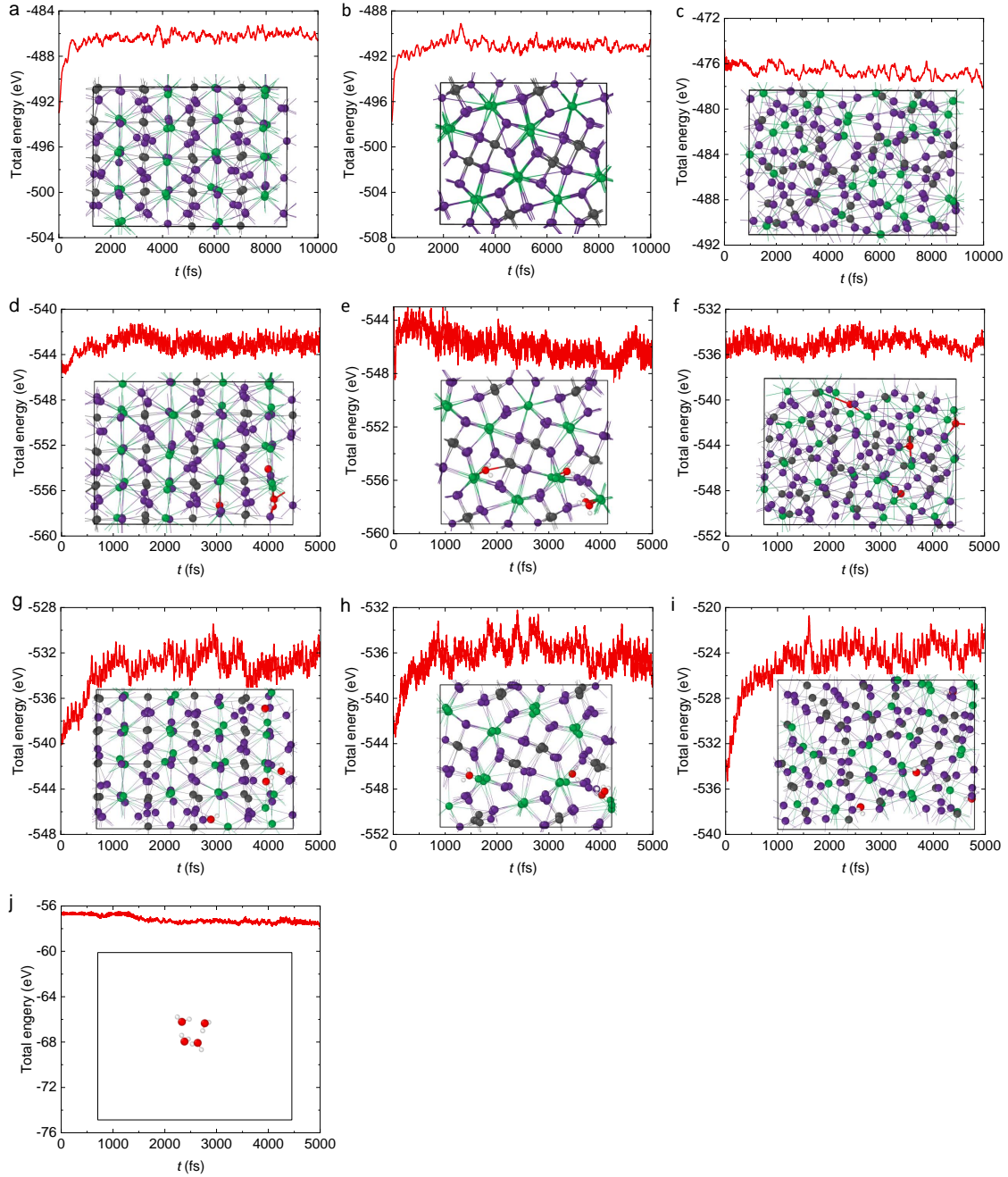


FIG. S13. **Structures and time evolution of the total energies in AIMD simulations for different systems at 300 K.** (a-c) CsPbI₃ in (a) Black phase, (b) Yellow phase, (c) Amorphous phase; (d-f) CsPbI₃ in (a) Black phase, (b) Yellow phase, (c) Amorphous phase with four water molecules; (g-i) CsPbI₃ in (a) Black phase, (b) Yellow phase, (c) Amorphous phase with four water molecules at 600 K; (j) Four water molecules in vacuum. The CsPbI₃ system includes 32 formula units.

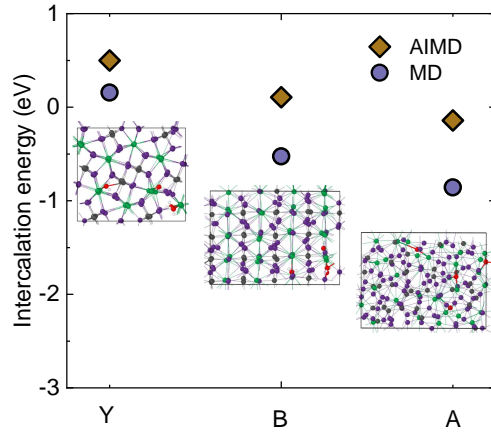


FIG. S14. A comparison of the structures and calculation results of intercalation energy of a single water molecule in black phase, yellow phase, and amorphous CsPbI_3 using AIMD and MD simulations.

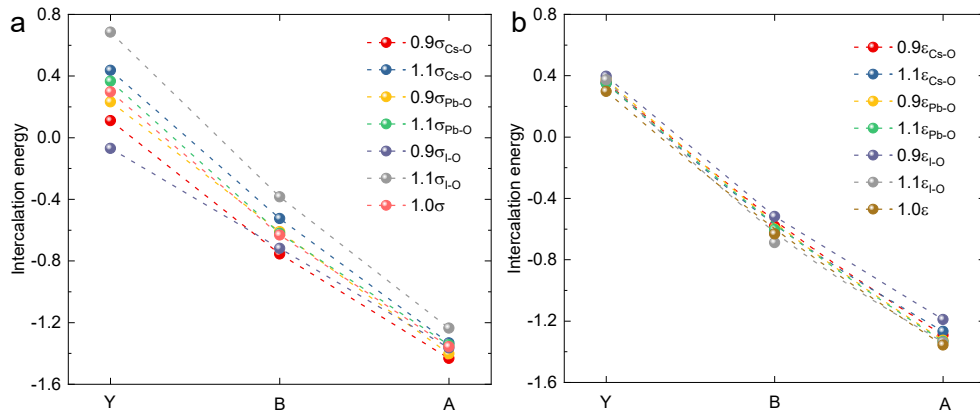


FIG. S15. Influence of scaling LJ parameters (a) σ and (b) ϵ on the intercalation energy.

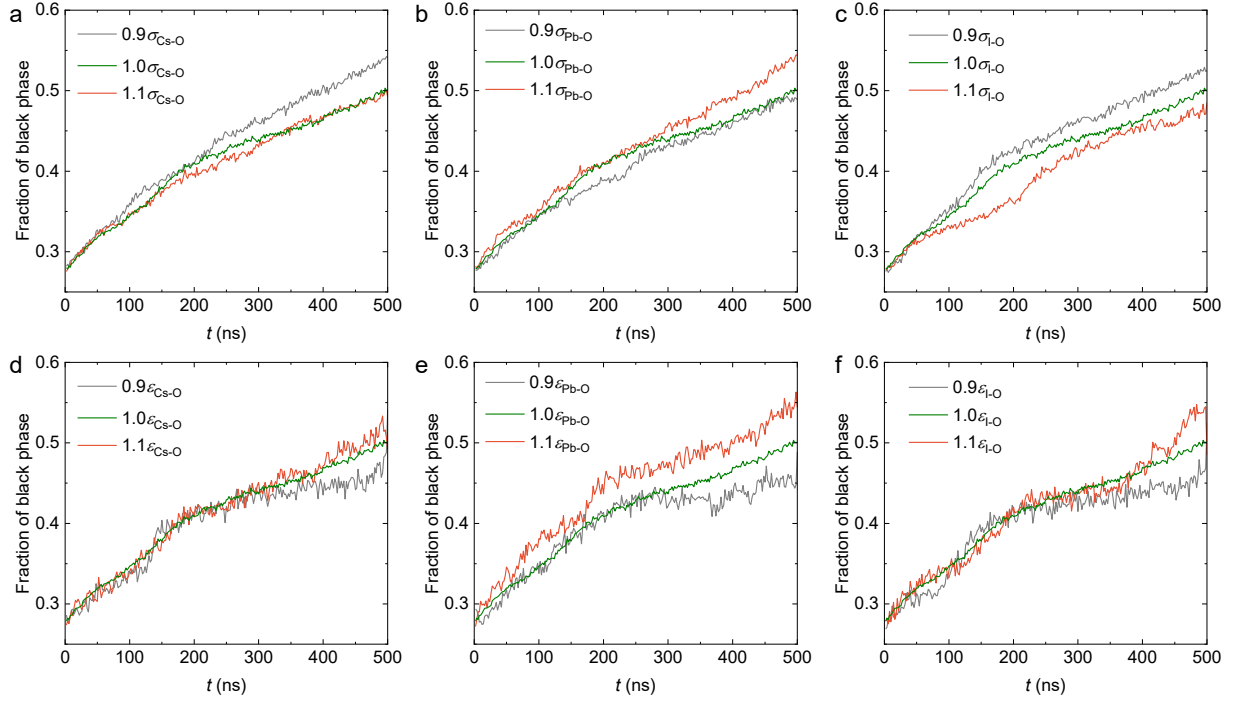


FIG. S16. **Influence of scaling LJ parameters σ and ϵ on the $Y \rightarrow B$ phase transition rate.** (a) σ_{Cs-O} , (b) σ_{Pb-O} , (c) σ_{I-O} , (d) ϵ_{Cs-O} , (e) ϵ_{Pb-O} , (f) ϵ_{I-O} .

TABLE I. Interfacial energies σ (in eV/nm²) of the black/yellow (B/Y), black/amorphous (B/A), Y/A, black/amorphous with water (B/A+w), and Y/A+w interfaces calculated by classical MD and AIMD

at 300 K, and that of the Y/A+w interface at 450 K.

Interfaces ^a	B/Y	B/A	Y/A	B/A+w	Y/A+w	Y/A+w, 450 K
MD	1.44	0.64	0.50	0.51	0.43	0.30
AIMD	1.51	0.47	0.45	-	-	-

^a 300 K if not stated.

TABLE II. Force field parameters for the CsPbI₃-water system.

Ions	ϵ (kJ/mol)	σ (nm)	q (e)
Cs ^a	7.456	0.3584	0.8600
Pb ^a	0.1048	0.3210	0.8500
I ^a	6.164	0.4014	-0.5700
O ^b	14.984	0.3166	-0.8476
H ^b	0.0000	0.0000	0.4238

^a Ref. 4.

^b Ref. 5.

TABLE III. Cutoff radii (in Å) used in the coordination number calculations.

Ion pairs	Cs-I	Pb-I	Cs-Pb	Cs-O	Pb-O	I-O
Cutoff	6.00	4.45	6.40	5.00	3.75	5.45

TABLE IV. Key properties of CsPbI₃ polymorphs predicted by the force field, together with experimental and DFT results for comparison. Lattice parameters a , b , and c are in Å; Transition temperatures T are in K; Relative energies ΔE are in eV/f.u..

Phases	Properties	Force field ^a	Expt. ^b	DFT ^c
α	a	6.22	6.30	6.30
	$T_{\beta \rightarrow \alpha}$	680	550	–
	$T_{\delta \rightarrow \alpha}$	450	580	–
	T_m	810	745	–
β	a	8.62	8.83	8.72
	b	6.42	6.30	6.42
	$T_{\gamma \rightarrow \beta}$	500	457	–
	$\Delta E_{\alpha-\beta}$	0.072	–	0.068
γ	a	8.31	8.62	8.50
	b	9.11	8.85	9.04
	c	12.56	12.50	12.54
	$\Delta E_{\beta-\gamma}$	0.031	–	0.39
δ	a	4.99	4.80	4.82
	b	10.38	10.45	10.60
	c	17.72	17.76	17.93
	$\Delta E_{\gamma-\delta}$	0.048	–	0.132

^a Refs 4, 7.

^b Refs 27.

^c Refs 4, 16.

Movie S1: Trajectories of water molecules binding with the Cs and Pb ions at the B/Y interface from classical MD simulations.

REFERENCES

- ¹H. J. Berendsen, D. van der Spoel, and R. van Drunen, “Gromacs: A message-passing parallel molecular dynamics implementation,” *Comput. Phys. Commun.* **91**, 43–56 (1995).
- ²W. C. Swope, H. C. Andersen, P. H. Berens, and K. R. Wilson, “A computer simulation method for the calculation of equilibrium constants for the formation of physical clusters of molecules: Application to small water clusters,” *J. Chem. Phys.* **76**, 637–649 (1982).
- ³G. J. Martyna, D. J. Tobias, and M. L. Klein, “Constant pressure molecular dynamics algorithms,” *J. Chem. Phys.* **101**, 4177–4189 (1994).
- ⁴C. G. Bischak, M. Lai, Z. Fan, D. Lu, P. David, D. Dong, H. Chen, A. S. Etman, T. Lei, J. Sun, *et al.*, “Liquid-like interfaces mediate structural phase transitions in lead halide perovskites,” *Matter* **3**, 534–545 (2020).
- ⁵H. J. Berendsen, J. R. Grigera, and T. P. Straatsma, “The missing term in effective pair potentials,” *J. Phys. Chem.* **91**, 6269–6271 (1987).
- ⁶T. Darden, D. York, and L. Pedersen, “The effect of long-range electrostatic interactions in simulations of macromolecular crystals—a comparison of the ewald and truncated list methods,” *J. Chem. Phys.* **99**, 10089 (1993).
- ⁷X. Hao, J. Liu, M. Deng, and Z. Fan, “Critical evaluation of five classical force fields for CsPbI₃: limitations in modeling phase stability and transformations,” *J. Phys. Chem. C* **127**, 20157–20168 (2023).
- ⁸E. Fransson, J. Wiktor, and P. Erhart, “Phase transitions in inorganic halide perovskites from machine-learned potentials,” *J. Phys. Chem. C* **127**, 13773–13781 (2023).
- ⁹X. Luo, W. Liu, Z. Wang, T. Lei, P. Yang, and Y. Yu, “Thermally driven phase transition of halide perovskites revealed by big data-powered in situ electron microscopy,” *J. Chem. Phys.* **158** (2023).
- ¹⁰P. M. Larsen, “Revisiting the common neighbour analysis and the centrosymmetry parameter,” arXiv preprint arXiv:2003.08879 (2020).
- ¹¹A. Stukowski, “Visualization and analysis of atomistic simulation data with OVITO—the open visualization tool,” *Modell. Simul. Mater. Sci. Eng.* **18**, 015012 (2009).

- ¹²G. Kresse and J. Furthmüller, “Efficiency of ab-initio total energy calculations for metals and semiconductors using a plane-wave basis set,” *Comput. Mater. Sci.* **6**, 15–50 (1996).
- ¹³G. Kresse and D. Joubert, “From ultrasoft pseudopotentials to the projector augmented-wave method,” *Phys. Rev. B* **59**, 1758–1775 (1999).
- ¹⁴S. Grimme, J. Antony, S. Ehrlich, and H. Krieg, “A consistent and accurate ab initio parametrization of density functional dispersion correction (DFT-D) for the 94 elements H-Pu,” *J. Chem. Phys.* **132**, 154104 (2010).
- ¹⁵S. Grimme, S. Ehrlich, and L. Goerigk, “Effect of the damping function in dispersion corrected density functional theory,” *J. Comput. Chem.* **32**, 1456–1465 (2011).
- ¹⁶T. Braeckevelt, R. Goeminne, S. Vandenhoute, S. Borgmans, T. Verstraelen, J. A. Steele, M. B. Roeffaers, J. Hofkens, S. M. Rogge, and V. Van Speybroeck, “Accurately determining the phase transition temperature of CsPbI₃ via random-phase approximation calculations and phase-transferable machine learning potentials,” *Chem. Mater.* **34**, 8561–8576 (2022).
- ¹⁷M. Parrinello and A. Rahman, “Polymorphic transitions in single crystals: A new molecular dynamics method,” *J. Appl. Phys.* **52**, 7182–7190 (1981).
- ¹⁸R. Jinnouchi, J. Lahnsteiner, F. Karsai, G. Kresse, and M. Bokdam, “Phase transitions of hybrid perovskites simulated by machine-learning force fields trained on the fly with bayesian inference,” *Phys. Rev. Lett.* **122**, 225701 (2019).
- ¹⁹R. Jinnouchi, F. Karsai, and G. Kresse, “On-the-fly machine learning force field generation: Application to melting points,” *Phys. Rev. B* **100**, 014105 (2019).
- ²⁰A. P. Bartók, M. C. Payne, R. Kondor, and G. Csányi, “Gaussian approximation potentials: The accuracy of quantum mechanics, without the electrons,” *Phys. Rev. Lett.* **104**, 136403 (2010).
- ²¹S. Dastidar, C. J. Hawley, A. D. Dillon, A. D. Gutierrez-Perez, J. E. Spanier, and A. T. Fafarman, “Quantitative phase-change thermodynamics and metastability of perovskite-phase cesium lead iodide,” *J. Phys. Chem. Lett.* **8**, 1278–1282 (2017).
- ²²G.-Y. Chen, Z.-D. Guo, X.-G. Gong, and W.-J. Yin, “Kinetic pathway of γ -to- δ phase transition in CsPbI₃,” *Chem* **8**, 3120–3129 (2022).
- ²³W. Yang, J. Li, X. Chen, Y. Feng, C. Wu, I. D. Gates, Z. Gao, X. Ding, J. Yao, and H. Li, “Exploring the effects of ionic defects on the stability of CsPbI₃ with a deep learning potential,” *ChemPhysChem* **23**, e202100841 (2022).
- ²⁴T. Braeckevelt, R. Goeminne, S. Vandenhoute, S. Borgmans, T. Verstraelen, J. A. Steele, M. B. Roeffaers, J. Hofkens, S. M. Rogge, and V. Van Speybroeck, “Accurately determining the

- phase transition temperature of CsPbI₃ via random-phase approximation calculations and phase-transferable machine learning potentials,” *Chem. Mater.* **34**, 8561–8576 (2022).
- ²⁵Y. Sun, D. Zhang, A. Bashir, C. Li, and Z. Fan, “Scaling solute–solvent distances to improve solubility and ion pairing predictions in rigid ion models,” *J. Phys. Chem. B* **127**, 9575–9586 (2023).
- ²⁶S. Blazquez, M. Conde, and C. Vega, “Scaled charges for ions: An improvement but not the final word for modeling electrolytes in water,” *J. Chem. Phys.* **158**, 054505 (2023).
- ²⁷A. Marronnier, G. Roma, S. Boyer-Richard, L. Pedesseau, J.-M. Jancu, Y. Bonnassieux, C. Katan, C. C. Stoumpos, M. G. Kanatzidis, and J. Even, “Anharmonicity and disorder in the black phases of cesium lead iodide used for stable inorganic perovskite solar cells,” *ACS Nano* **12**, 3477–3486 (2018).